Mass-Guided Single-Cell MALDI Imaging of Low-Mass Metabolites Reveals Cellular Activation Markers

James L. Cairns, Johanna Huber, Andrea Lewen, Jessica Jung, Stefan J. Maurer, Tobias Bausbacher, Stefan Schmidt, Pavel A. Levkin, Daniel Sevin, Kerstin Göpfrich, Philipp Koch, Oliver Kann, and Carsten Hopf*

Single-cell MALDI mass spectrometry imaging (MSI) of lipids and metabolites >200 Da has recently come to the forefront of biomedical research and chemical biology. However, cell-targeting and metabolome-preserving methods for analysis of low mass, hydrophilic metabolites (<200 Da) in large cell populations are lacking. Here, the PRISM-MS (PRescan Imaging for Small Molecule – Mass Spectrometry) mass-guided MSI workflow is presented, which enables space-efficient single cell lipid and metabolite analysis. In conjunction with giant unilamellar vesicles (GUVs) as MSI ground truth for cell-sized objects and Monte Carlo reference-based consensus clustering for data-dependent identification of cell subpopulations, PRISM-MS enables MSI and on-cell MS2-based identification of low-mass metabolites like amino acids or Krebs cycle intermediates involved in stimulus-dependent cell activation. The utility of PRISM-MS is demonstrated through the characterization of complex metabolome changes in lipopolysaccharide (LPS)-stimulated microglial cells and human-induced pluripotent stem cell-derived microglia. Translation of single cell results to endogenous microglia in organotypic hippocampal slice cultures indicates that LPS-activation involves changes of the itaconate-to-taurine ratio and alterations in neuron-to-glia glutamine-glutamate shuttling. The data suggests that PRISM-MS can serve as a standard method in single cell metabolomics, given its capability to characterize larger cell populations and low-mass metabolites.

1. Introduction

Recent advances in spatial- and mass resolution, in state-of-the-art machine learning, and in on-tissue tandem-MS (MS2) fragmentation analysis for metabolite identification and increased molecular specificity in matrix-assisted laser desorption/ionization (MALDI) trapped ion mobility spectrometry (tims) or Fourier transform mass spectrometry imaging (MSI) have propelled MALDI imaging to the forefront of biomedical research.[1] MSI has enabled detailed single-cell analysis within populations of cultured cells or mixtures of cell types.[2] Furthermore, population statistics of cultured cells has been assessed by MSI at the single-cell level.[2d–f,3]

These single-cell platforms either scan entire slides by MSI, which is time-consuming, or smaller fields per slide, thus limiting throughput, or microarrays that hold single cells per spot.[2e,3b,4] Alternatively, they use image-guidance, i.e., orthogonal imaging technologies such as fluorescence microscopy or bright field

J. L. Cairns, J. Huber, T. Bausbacher, S. Schmidt, C. Hopf
Center for Mass Spectrometry and Optical Spectroscopy
CeMOS
Mannheim University of Applied Sciences
68163 Mannheim, Germany
E-mail: c.hopf@hs-mannheim.de
J. L. Cairns, C. Hopf
Medical Faculty
Heidelberg University
69120 Heidelberg, Germany

A. Lewen, O. Kann
Institute of Physiology and Pathophysiology
Heidelberg University
69120 Heidelberg, Germany
J. Jung, P. Koch
Dept. Translational Brain Research
Central Institute for Mental Health (CIMH)
68159 Mannheim, Germany
J. Jung, P. Koch
German Cancer Research Center (DKFZ)
69120 Heidelberg, Germany
J. Jung, P. Koch
Hector Institute for Translational Brain Research (HITBR gGmbH)
68159 Mannheim, Germany

scanning, to identify cell positions first, and then perform directed cell MSI in the second step.[2d,3a,c,5] However, current MSI-based single cell metabolomics platforms focus on lipidomics and only occasionally on metabolites >200 Da,[2e] and they do not cover hydrophilic metabolites with masses below 200 Da such as TCA cycle metabolites or amino acid catabolites.

Minimizing metabolic alterations for mass spectrometry imaging of cells involves addressing two critical factors: (i) the use of fixative agents, such as paraformaldehyde (PFA), which can lead to metabolite extraction during fixation and washing, and (ii) reducing the exposure of unfixed cells to environmental factors such as light and heat, particularly during the extended microscopic prescanning step typically conducted under ambient conditions. Most MSI-based platforms use paraformaldehyde (PFA)-fixed cells.[2e,4b,5,6]

Here, we introduce the PRISM-MS (PRescan Imaging for Small Molecule – Mass Spectrometry) workflow and a software package that omits PFA fixation and combines a fast and metabolite-preserving low spatial resolution (≥100 µm) MSI PreScan with a higher spatial resolution (≤20 µm) MSI DeepScan into a mass-guided single cell MSI workflow. Utilizing giant unilamellar vesicles (GUVs) as cell-sized model membrane systems with known molecular composition as an analytical ground truth,[7] we validate Monte Carlo reference-based Consensus Clustering (M3C) as an automatable approach for selection of cell subpopulations. We translate PRISM-MS with M3C into a search for microglial metabolite activation markers in microglial-like cells, hiPSC-derived microglial cell lines and finally in rat organotypic hippocampal slice cultures.

It has been noted for many years that microglia, arguably in conjunction with reactive astrocytes, play a pivotal role in neurodegeneration, in particular in Alzheimer's disease (AD).[8]

S. J. Maurer, K. Göpfrich
Biophysical Engineering Group
Center for Molecular Biology of Heidelberg University (ZMBH)
69120 Heidelberg, Germany
S. J. Maurer, K. Göpfrich
Biophysical Engineering Group
Max-Planck Institute for Medical Research
69120 Heidelberg, Germany
P. A. Levkin
Institute of Biological and Chemical Systems – Functional Molecular Systems (IBCS-FMS)
Karlsruhe Institute of Technology
76344 Karlsruhe, Germany
P. A. Levkin
Institute of Organic Chemistry
Karlsruhe Institute of Technology
76344 Karlsruhe, Germany
D. Sevin
Cellzome – A GSK company
69115 Heidelberg, Germany
P. Koch, C. Hopf
Mannheim Center for Translational Neuroscience (MCTN)
Heidelberg University
68167 Mannheim, Germany
O. Kann
Interdisciplinary Center for Neurosciences (IZN)
Heidelberg University
69120 Heidelberg, Germany

Besides surveying and activated microglia, multiple states of microglial cells characterized by distinct, but complex transcriptomic, proteomic, and metabolomic signatures coexist.[9] However, most molecular studies to date have focused on transcriptomics and proteomics, whereas microglial cellular metabolomics remains understudied.[10] For instance, in-depth transcriptomics analysis of LPS-stimulated cultured primary mouse microglia, in vivo LPS-treated microglia, and human induced pluripotent stem cells (hiPSCs) suggested species differences in metabolic reprogramming during induction of inflammatory responses.[11] Striking changes included alterations in cytokine production, glycolysis or the TCA cycle. For instance, conversion of aconitate to α-ketoglutarate was deregulated post-LPS-exposure.[11] During microglial activation aconitate is decarboxylated to itaconate, the immune cell-specific "poster-child of metabolic reprogramming", to create a pro-inflammatory response.[12] Liquid-chromatography (LC-)MS metabolomics, albeit not at a single-cell level, has recently identified metabolite changes associated with microglia activation in the multiple sclerosis-like experimental autoimmune encephalomyelitis (EAE) model in mice.[13] LC-MS metabolomics highlighted changes in amino acid, taurine, and itaconate levels – the latter also demonstrated by DESI-MS imaging – and in other metabolites associated with energy metabolism, oxidative stress, and mitochondrial function.[13] Taurine is known to reduce microglia activation in brain.[14]

We therefore demonstrate the utility of the PRISM-MS single-cell MALDI imaging platform in discovery and MS2 characterization of cellular markers of LPS-induced microglia activation.

2. Results

2.1. PRISM-MS for Low Mass Metabolite-Preserving and Single Cell-Focused Spatial Metabolomics

PRISM-MS utilizes two subsequent scans – a PreScan at low spatial resolution (≥100 µm) that can employ any cell marker like FA18:1 (m/z 281.25 [M-H]$^-$) for fast, whole-slide identification of cell containing spots. A subsequent DeepScan at high spatial resolution (≤20 µm) is restricted to cell-containing PreScan fields (**Figure 1a,b**; Figure S1, Supporting Information). For cultures with intermediate cell density (1000 cells/cm^2), we noted a 12-fold speed advantage and concomitant reduction of file size (50 instead of 600 GB; Figures S2 and S3, Supporting Information) compared to whole-slide scans at 20 µm. The more 200 µm PreScan pixels are devoid of cells, the higher the speed and file size advantage. The user-selected pixel-size of the DeepScan is typically ≤20 µm. PRISM-MS works well with both light-transmitting slides (e.g., glass or ITO chamber slides or droplet microarrays[15]) and non-light-transmitting slides (such as gold-coated slides) (Figures S4–S6, Supporting Information). Furthermore, PRISM-MS can combine different modalities such as positive and negative ion modes, and it is compatible with on-tissue data-dependent fragmentation analysis for metabolite identification, e.g., MALDI-imaging parallel reaction monitoring-parallel accumulation serial fragmentation (iprm-PASEF)[1d] or MALDI-TIMS-MS2-MSI approaches.[1b]

PRISM-MS users can adjust two scanning parameters (Figure S7, Supporting Information): A) the dilution factor
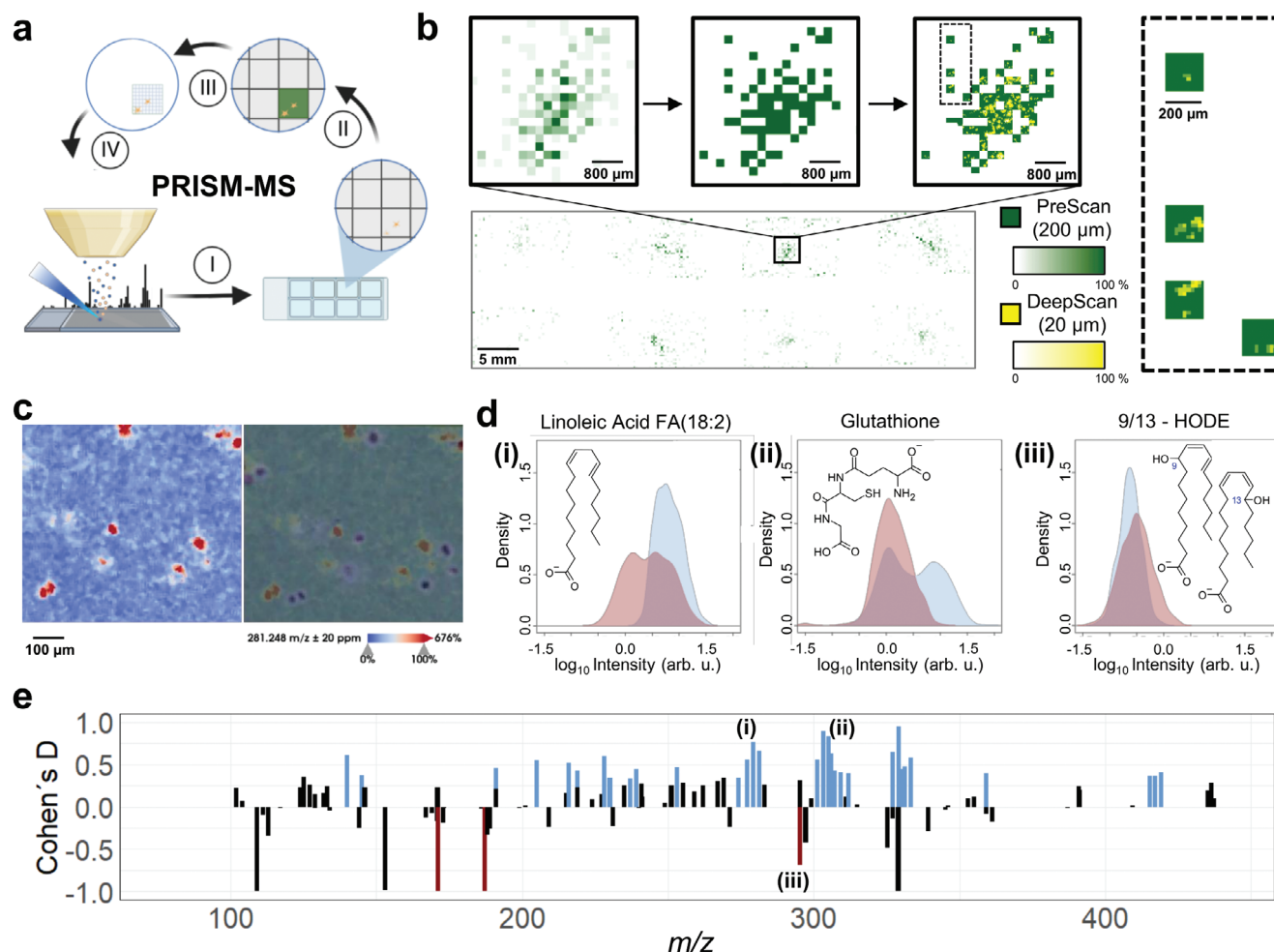
2410506 (2 of 15)

Figure 1. PRISM-MS for fast low mass metabolite-preserving single-cell spatial metabolomics. a) Schematic overview of PRISM-MS workflow. (I) Survey PreScan at large (e.g., >100 µm) pixel size; (II) determine cell containing pixels by feature-selective binary image segmentation; (III) definition of cell containing pixels as new measurement regions; (IV) DeepScan at small (e.g., <20 µm) pixel size; followed by data analysis for single cell metabolomics and cluster detection (Figure S13, Supporting Information). b) PRISM-MS example of cultured SIMA9 mouse microglia cells covered with MALDI matrix directly after lyophilization: the PreScan obtains cellular signal intensities per 200-µm pixels (green color scale) (upper panel left), which then get thresholded (upper panel middle) and undergo a subsequent DeepScan at 20-µm pixel size to resolve individual cells (upper panel right). Right dashed box: four distinct 200-µm measurement regions with 20 µm DeepScan step size (ion images of m/z 281.25 (FA 18:1 [M-H]$^-$)). c) Left panel: 5-µm MSI image of cell marker m/z 281.25 (FA 18:1 [M-H]$^-$); right panel: overlay of ion image with haematoxylin and eosin (H&E) -stained slide generated after MSI. The registration offset is deliberate, in order to demonstrate cell identification versus H&E ground truth. d) Intensity profiles for (i) m/z 279.23 (linoleic acid [M-H]$^-$), (ii) m/z 306.08 (glutathione [M-H]$^-$) and (iii) m/z 295.23 (9- and 13-hydroxy-octadecadienoic acids (9/13-HODE) [M-H]$^-$) obtained by PRISM-MS (blue) versus the optically guided workflow (red). Oxidation of linoleic acid to 9/13-HODE is reduced in PRISM-MS. e) PRISM-MS preserves metabolite profiles: average ($N = 3$) Comparison of Cohen's D effect sizes for small molecule m/z features obtained by PRISM-MS or by a workflow including 30 min slide exposure to ambient conditions to emulate workflows that capture, e.g., a high resolution optical image before MSI.[3c] Metabolites with significantly higher (blue) or lower (red) effect sizes/ intensities in PRISM-MS versus emulated optically guided workflow. Black bars indicate peaks with non-significant ($p > 0.05$; $N = 3$ each for PRISM and emulated optical workflow) differences between the workflows.

computationally dilates PreScan pixels before the DeepScan, in order to avoid capturing incomplete cells (Figure S1, Supporting Information). B) The intensity threshold that is commonly defined by the mean intensity for the target m/z (e.g., m/z 281.25) ± 1 to 2.5 standard deviations. This ensures that most cells seeded on the slide are captured. It is subsequently listed as the number of standard deviations (α).

Fluorescence scans of Hoechst-stained SIMA9 microglia cells or H&E-stained cells (Figure 1c) as a ground truth for absence or presence of cells suggested that false positive/negative rates

could effectively be fine-tuned using these parameters (Figures S7 and S8, Supporting Information), resulting in different file sizes (Figure S3, Supporting Information). For example, with a dilation factor of 1 and a threshold of $T_N = 1$, the false-positive and false-negative rates for cell ID in MSI were typically 6.5% and 76.7%, respectively. With a dilation factor of 1 and threshold $T_N = 3$, the false-positive and false-negative rates for cell ID in MSI were typically 1.9% and 90.1%, respectively.

The driving force behind development of PRISM-MS was the need to cover metabolites with m/z below 200 that are of major

interest in metabolomics and to improve metabolite preservation throughout sample preparation and imaging (Figure S9, Supporting Information). Most single cell MSI metabolomics workflows use PFA-fixed cells. This type of fixation may increase imaging quality for single cell lipidomics, but it causes leakage of cytosolic hydrophilic compounds.[2f] These metabolites may be reduced by 90% after PFA-fixation.[2d] In addition, during optical-guidance-based MSI approaches, extended incubation of cells at room temperature during acquisition of high-resolution microscopic images that define cell positions may also cause undesired metabolome alterations (Figure 1e).

In contrast, we chose to fix cultured cells on slides by immediate lyophilization and by covering them with UV-shielding MALDI matrix chemicals and fixing organic solvents as quickly as possible to preserve the metabolomic state. Lyophilization can immobilize molecules inside samples within milliseconds.[16] Interestingly, recent mass cytometry-based single-cell metabolomics methods also use non-PFA-fixed cells.[17]

Comparison of PRISM-MS with a 30 min incubation of unfixed cells at room temperature prior to MSI to emulate an optically guided workflow led to substantially different metabolite profiles, calculated as Cohen's D, a standardized effect size for assessing the difference between two groups (Figure 1e). Cells assessed via microscopic guidance may not represent stable metabolomes, as they are exposed to heat, UV-light (not being shielded by MALDI matrix), and oxygen during extended optical scanning. In PRISM-MS, glutathione depletion, oxidation of linoleic acid to bioactive pathology-associated 9- or 13- hydroxy-octadecadienoic acids (9/13-HODE; Figure 1d) and oxidation of additional polyunsaturated fatty acids (Figure S10, Supporting Information) were all reduced compared to an emulated optically guided workflow.[18] PRISM-MS also led to a slightly higher total number of false-discovery rate (FDR)-controlled metabolite annotations in METASPACE[19] (Figure S11, Supporting Information), whilst not affecting spectral quality in general (Figure S12, Supporting Information).

As PRISM-MS provides an MSI-only analysis with higher speed and improved metabolite preservation compared to microscopy-based imaging, it requires rather low cell culture seeding densities of 1000 cells per cm^2. The PRISM-MS data processing pipeline i) clusters MSI pixels into "cells"/objects, then ii) distinguishes single cells from cell aggregates/conglomerates, and iii) removes the latter from consideration. In such low-density cell cultures, up to seven pixels, most of which contain only a small portion of the cell, can be clustered together to define a single cell, and such cultures typically contain >90% single cells (Figure S13, Supporting Information).

2.2. Giant Unilamellar Vesicles (GUVs) as Analytical Ground Truth for Monte Carlo Reference-Based Consensus Clustering (M3C) of Cell Subpopulations in PRISM-MS

GUVs are cell-sized model membrane systems characterized by their defined lipid constituents. Given that the subset of metabolites present in any set of cells is generally unknown, the lack of that ground truth often complicates the testing of new models or algorithms. We therefore reasoned that

GUVs could serve as a (qualitative) ground truth in MSI to validate the PRISM-MS single cell analysis pipeline. We employed two types of single-lipid GUVs composed of 1,2-dioleoyl-sn-glycero-3-phosphocholine (DOPC) and 1,2-dimyristoyl-sn-glycero-3-phosphocholine (DMPC) with heterogeneous size-distributions of up to 50 µm in diameter and a mixture of the two GUV types (**Figure 2a–c**; Figures S14 and S15, Supporting Information).[7] As a control, we included 1% lissamine rhodamine B-labeled phosphatidylethanolamine in the lipid mixture. Colocalization of fluorescence label and DOPC MSI ion image of dual-labeled GUVs confirmed that the PRISM-MS DeepScan effectively detected and characterized these structures (Figure 2d).

Using the GUV ground truth data, we evaluated a recent clustering algorithm, Monte Carlo reference-based Consensus Clustering (M3C) that had not been used in MSI yet. In popular clustering methods like k-means clustering the number of classes k is either arbitrarily picked or inferred according to the Calinski-Harabasz criterion,[20] Xie-Beni, Davies-Bouldin,[21] Silhouette Criterion,[22] or the GAP statistic.[23] M3C was developed to detect heterogeneities in genomic data and to avoid expectation bias.[24] For high dimensional data like genomic or MSI data M3C repeats a statistical test for various k values, for instance, 200 times (as in Monte Carlo simulations), and identifies those k that show significant differences from a homogeneous distribution. The algorithm then evaluates a reference cluster stability index (RCSI) for all significant k values. The most stable k is ultimately used for segmentation.[24] M3C outperforms traditional clustering evaluation metrics by not only determining whether subclusters deviate significantly from random distributions through p-values but also by identifying the most stable clustering solution over multiple simulations, making it more robust for noisy datasets like in MSI (Figures S16 and S17, Supporting Information).

We analyzed DOPC-only and DMPC-only GUVs and a 1:1 mixture of the two GUV types by PRISM-MS. For both lipid m/z tested separately, the RCSI in M3C was highest for k = 2 subpopulations suggesting that m/z for both DOPC and DMPC were not evenly distributed across the entire population (Figure 2e,f). This analysis suggested four possible groups and labels: DOPC-/DMPC+ (1), DOPC+/DMPC- (2), DOPC+/DMPC+ (3), and DOPC-/DMPC- (not observed). Even in the mixture, most GUVs were classified as (1) or (2) (Figure 2g–i). The small number of vesicles in the mixture classified as positive for both (3) were typically two vesicles in close proximity that were not separable at 20 µm lateral step size (Figure 2f,i; Figure S18, Supporting Information). Most GUVs were represented by a single 20-µm pixel. Even though GUV sizes varied (Figure S15, Supporting Information), size differences did not affect their group assignment (Figure S18, Supporting Information). Annotation of molecular differences between DOPC-/DMPC+ (1) and DOPC+/ DMPC- (2) clusters in METASPACE followed by MS2 fragmentation analysis revealed 13 features including a DOPC fragment, LysoPC (18:1) (Figure 2j,k). As expected and as a validation of the approach, both lipids including variants such as their sodium adducts were specific for their own cluster. Besides serving as a qualitative ground truth, GUVs together with stable isotope-labeled standards may in the future form the basis for lipid quantification in single-cell MSI.[3b]
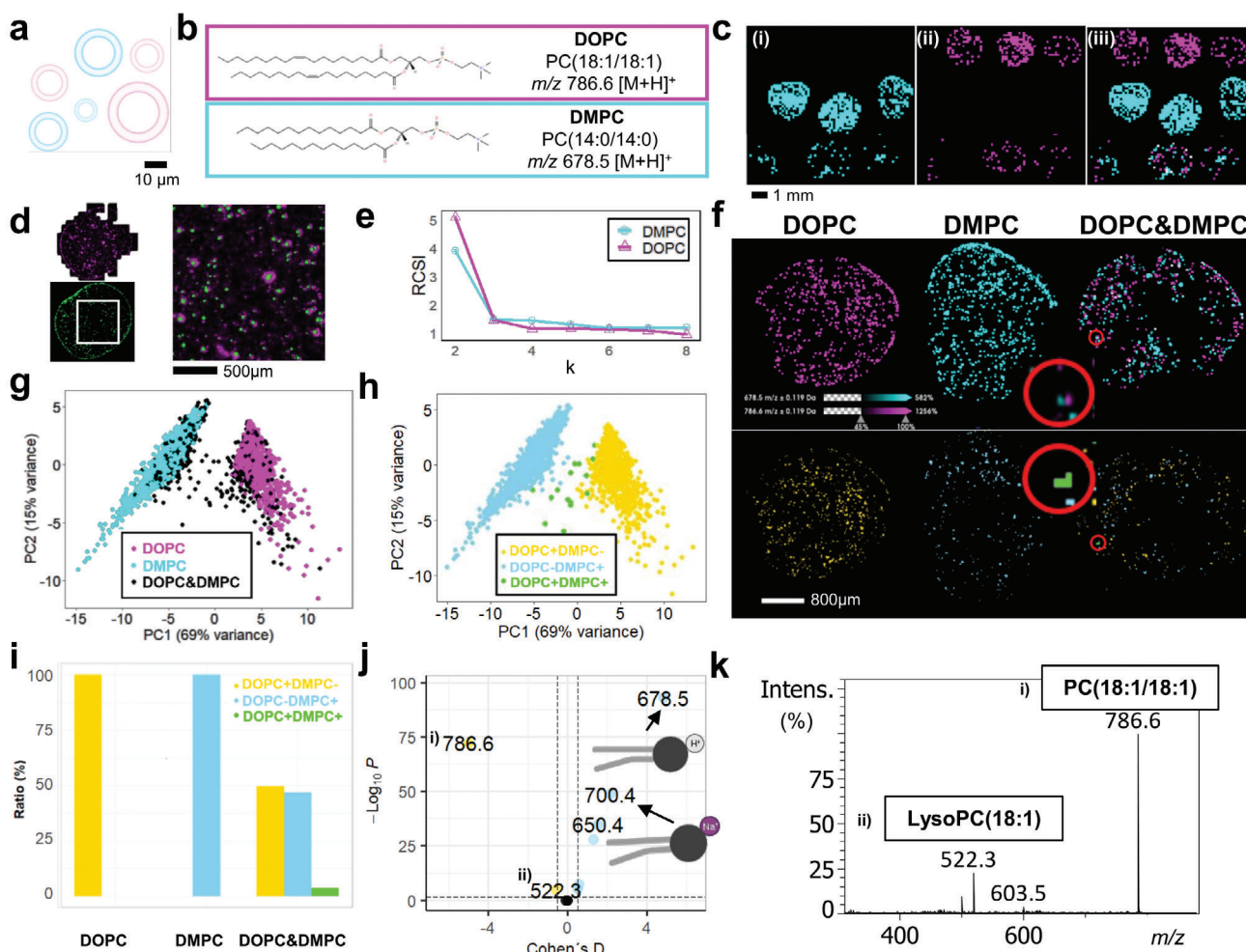
Figure 2. Giant unilamellar vesicles (GUVs) as an analytical ground truth for validation of Monte Carlo Consensus Clustering (M3C). a) GUVs are 5–50 µm single-lipid vesicles composed of either DOPC (magenta) or DMPC (cyan). b) Chemical structures of protonated DOPC (m/z 786.6; phosphatidylcholine PC(18:1/18:1) [M+H]$^+$) and DMPC (m/z 678.5; PC(14:0/14:0) [M+H]$^+$). c) Binary thresholded image of the PRISM-MS 200-µm PreScan displayed for (i) DOPC, (ii) DMPC, and (iii) a 1:1 mixture of both GUV types. Three spots each were applied onto ITO slides. d) Overlay of fluorescence image of lissamine rhodamine B (red; 1% LissRhod-PE included in lipid mixture) label in GUVs, and 20-µm pixel DeepScan of m/z 786.6 (DOPC; cyan). e) Monte Carlo Consensus Clustering (M3C) for a 1:1 mixture of DOPC and DMPC GUVs on a full ITO chamber slide. Relative Cluster Stability Index (RSCI) suggests k = 2, consistent with two classes of GUVs, as the most stable cluster with an overall $p < 0.01$. f) Top row – the ground truth: ion image overlays of m/z 786.6 (DOPC) and m/z 678.5 (DMPC) for three conditions: pure DOPC-, pure DMPC- and mixed DOPC/DMPC GUVs. Bottom row – M3C model generation: M3C clustering (k = 2) classifies GUVs as DOPC+ (yellow), DMPC+ (blue) or DOPC+/ DMPC+ (green). g) Principal component analysis (PCA) of GUVs; plot of PC1 and PC2 for the three conditions, DOPC (magenta), DMPC (cyan), and mixed DOPC/DMPC (black). h) Post-clustering PCA of GUVs categorized by the M3C model enables class assignment for each GUV: DOPC+/DMPC- (yellow), DOPC-DMPC+ (blue), and DOPC+DMPC+ (green). i) M3C model-based population statistics for the three conditions in (g) suggests that 3.5% of GUVs in DOPC/DMPC mixture are classified as DOPC+DMPC+. j) Cohen's D effect sizes versus p-value Volcano Plot for M3C cluster analysis: m/z features specific to DMPC-GUV populations, such as m/z 678.5 (DMPC [M+H]$^+$) and m/z 700.5 (DMPC [M+Na]$^+$), or specific to DOPC-GUV populations like m/z 786.6 (DOPC [M+H]$^+$) and the corresponding lysophosphatidylcholine (LPC) m/z 522.3. Benjamini-Hochberg adjusted p-value threshold was set to 0.05 and Cohen's D threshold to ± 0.2. k) MS2 spectrum of (i) m/z = 786.6 indicating (ii) LPC(18:1) [M+H]$^+$ as a likely DOPC fragment in j).

2.3. PRISM-M3C MS Reveals Sub-Population-Restricted Itaconate and Taurine Changes in Response to LPS Treatment in Microglia Cells

Following validation of the PRISM MS with M3C methodology in GUVs, we applied this approach to LPS-treated microglial cells in search for candidate activation markers in vitro. Non-confluent populations of SIMA9 microglial-like cells were treated with LPS (0 to 500 ng mL^{-1}). Activation was confirmed by TNFα-sandwich ELISA and did not affect cell viability (Figures S19–S21, Supporting Information). In contrast but as expected, EOC microglial cells lacking toll like receptor 4 (TLR4) did not respond to LPS and served as negative control. After the DeepScan (20 µm) in negative ion mode, single cells were inferred from up to seven connected pixels; larger areas of connected pixels were filtered out as likely cell aggregates, and candidate marker m/z were identified and annotated via METASPACE with FDR ≤10%. Several m/z were upregulated after LPS treatment (**Figure 3a**). Most
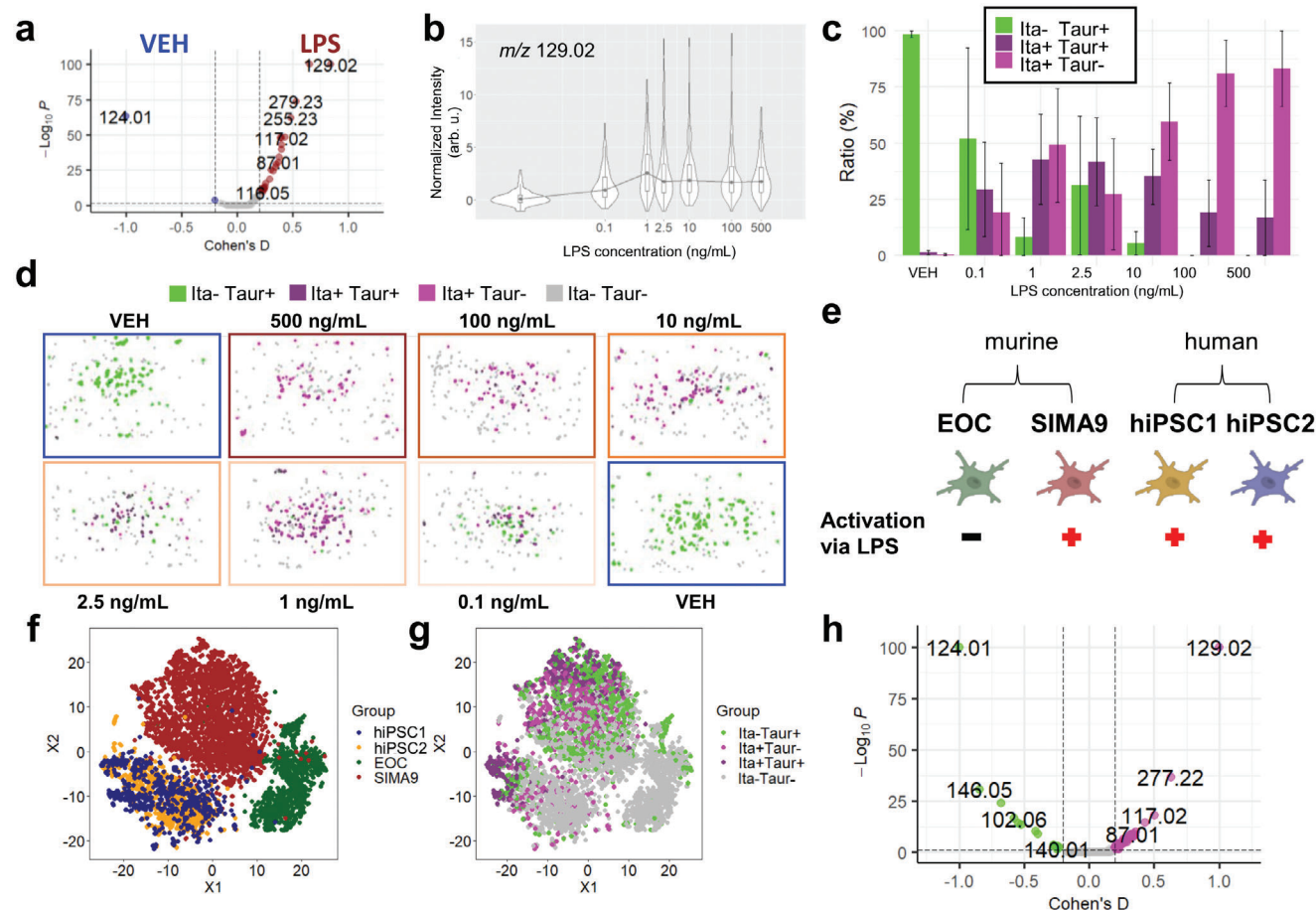
Figure 3. Microglial responses to LPS treatment revealed sub-populations of SIMA9 and hiPSC microglia cells. a) Modified Volcano plot for untreated (vehicle; VEH) and lipopolysaccharide (LPS) treated (500 ng mL^{-1}, 20 h) SIMA9 cells highlights m/z 124.01 (taurine [M-H]$^-$) and m/z 129.02 (itaconate [M-H]$^-$) as markers for non-activated and LPS-activated microglial cells, respectively. Benjamini-Hochberg adjusted p-value threshold was set to 0.05 and Cohen´s D threshold to ± 0.2. b) Itaconate violin plot: normalized intensity of itaconate per cell indicates microglial activation in correlation with LPS treatment. c) M3C cluster analysis of SIMA9 cells for itaconate and taurine labeling. Cells are categorized into four distinct groups by post analysis – itaconate-positive (Ita+Taur-, pink), taurine-positive (Ita-Taur+, green), and positive for both markers (Ita+Taur+, purple). Cells that don´t fall into either category (Ita-Taur-, grey) are omitted. d) Visualization of M3C cluster analysis for chamber slide wells untreated (VEH) or treated with a concentration range of LPS (0.1 to 500 ng mL^{-1}). e) Besides murine SIMA9 cells, the hiPSC-derived microglia cell lines hiPSC1 and hiPSC2 cells responded to LPS-treatment, as indicated by itaconate increases. Murine EOC cells lack toll-like receptor 4 and did not respond to LPS. f) t-distributed stochastic neighbor embedding (t-SNE) for the four microglial cells lines. g) t-SNE analysis of microglial activation status indicates that only a subset of SIMA9, hiPSC1, and hiPSC2 cells were activated by LPS (500 ng mL^{-1} for 20 h): Cells were categorized as Ita-Taur+ (green), Ita+Taur+ (purple), Ita+Taur- (pink), or Ita-Taur- (grey). EOC cells were non-reactive. h) Volcano plot restricted to Ita-Taur+ and Ita+Taur- cells. Comparing both clusters yielded more defined m/z-signatures for microglial activation (15 markers of non-activation and 55 activation marker candidates) than using cell pools (2 markers of non-activation and 26 activation markers; compare a) by reducing extraneous data. In total 8.878 cells were analysed and measured in six separate runs.

notably, the known microglial activation marker itaconate[25] (m/z 129.02; [M-H]$^-$) increased in a concentration-dependent manner (Figure 3a,b; Figure S19, Supporting Information). Of note, there are alternative annotations for m/z 129.02, e.g., the structural itaconate isomers gluconate and mesaconate, in the KEGG database, which are unlikely in this biological context, but could not be ruled out by MS2 fragmentation (Tables S1–S3; Dataset S1, Supporting Information). Interestingly, ion intensities (and presumed amounts of) itaconate in untreated cells were very low with low variance. In contrast, after LPS treatment some cells displayed very high intensities/levels (and many intermediate levels) of itaconate, whereas others stayed around zero, suggesting that the activation pattern was not homogenous

for all cells and that subpopulations may exist including dead cells (Figure 3b). The m/z 124.01, most prominent in untreated, widely non-activated microglial cells and decreasing in response to LPS was identified as taurine, a known inhibitor of lysine demethylase activity and of microglial activation by LPS[26] (Figure 3b; Figure S22, Supporting Information). All m/z were validated using high-resolution FTICR MS and MS^2 using SIRIUS (Tables S1–S3; Dataset S1, Supporting Information).[27]

We next applied M3C to PRISM-MS single-cell experiments. Using the activation-associated m/z for itaconate to check for cell activation, we noted k = 2 subpopulations (but k = 1 for EOC cells indicating no activation). k = 2 was also found for taurine, the marker of non-activated microglia, which led to four possible

**ADVANCED
SCIENCE NEWS**

www.advancedsciencenews.com

**ADVANCED
SCIENCE**
Open Access

www.advancedscience.com

labels for each single cell: taur+ita+, taur-ita+, taur+ita-, and taur-ita- (Figure 3c,d). The M3C approach can theoretically be extended to any (set of) *m/z* feature to identify subpopulations across all cells. However, performing this on a per-pixel level for MALDI imaging experiments, albeit feasible, would be very computationally intensive due to the large number of pixels considered. Using population statistics for the three of four subpopulations, we observed a shift from taurine-positive cells to itaconate-positive cells with increasing LPS concentration (Figure 3c). Taur-ita- cells (grey) were not considered for population statistics (Figure 3d). PRISM-MS with MC3 focusing on itaconate- and taurine-positive cells led to identification of 13 and 49 candidates for non-activation versus activation-specific biomarkers, respectively (Figure S23, Supporting Information). For validation, we expanded the M3C clustering and used all activation-specific cell markers from Figure 3a instead of just itaconate, which generated a similar pattern to itaconate clustering (Figure S24, Supporting Information).

Even though mouse SIMA9 cells have been used extensively as microglia surrogate as they display LPS responses,[28] their similarity with human microglia is rather limited. hiPSC-derived microglia may be a better model.[2g] We therefore extended PRISM MS with M3C analysis to two hiPSC cell lines (hiPSC1and hiPSC2), which in contrast to EOC cells also displayed itaconate increases in response to LPS (Figure 3e; Figure S25, Supporting Information). As for SIMA9, k = 2 resulted in the most stable clusters for the hiPSC lines and the same labels (taur+/ita+, taur-/ita+, taur+/ita- and taur-/ita-) were used. t-Distributed Stochastic Neighbor Embedding (t-SNE) analysis revealed a high degree of metabolomic similarity between both hiPSC cell lines and that EOC and SIMA9 cells were separate entities (Figure 3f). M3C-derived labels indicated that EOC cells were either non-activated or devoid of itaconate and taurine markers, whereas SIMA9 and the hiPSC lines were mixtures of cells belonging to any of the three subpopulations (taur+/ita+, taur-/ita+, taur+/ita-) (Figure 3g). M3C results for these three cell lines led to a refined taur-ita+ versus taur+ita- profile (Figure 3h; compare with Figure 3a) that disregarded unreactive and undefined cells in the analysis. Compared to the cell pool approach (Figure 3a), which identified 2 and 26 hits for non-activated versus LPS-treated cells, respectively, M3C analysis yielded 15 and 55 hits, respectively, from a total of 210 annotated *m/z* values – in addition to the information if a cell line was reactive to LPS or not (Figure 3h).

2.4. Translational Single Cell-Informed MALDI Imaging in Organotypic Hippocampal Slice Cultures Suggests Alterations in Metabolic Neuron-Glia Interplay in Response to LPS-Induced Neuroinflammation

We next tested if marker candidates identified by single-cell analysis in mouse and hiPSCs translated well to endogenous microglia in vivo or ex vivo. To avoid LPS-injections in vivo, we investigated M3C-derived microglial activation signatures in LPS-treated and then cryosectioned organotypic rat hippocampal slice cultures, which feature ramified and widely non-activated microglia.[29] In these tissue cultures, microglial activation can be reliably studied in the presence of functional neuron networks

and astrocyte syncytia.[30] Results can be compared with those gained in cell culture.

Slice cultures were split into three groups (**Figure 4a**): (1) Vehicle control (VEH) cultures were incubated for 72 h in medium, (2) the LPS group slices were treated with 1 µg mL⁻¹ LPS, and (3) the CLO group was exposed to 100 µg mL⁻¹ clodronate liposomes. This treatment results in effective depletion of microglial cells by ≈96% in slice cultures.[29c] These cells engulf the liposomes that, in turn, release clodronate intracellularly, thus stopping the TCA cycle and causing apoptosis.[29a,b,31] Five sets of slice cultures, with three conditions each, were subjected to MALDI-MSI. Comparison of Cohen's D effect sizes between the VEH- and LPS-treated groups highlighted 8 and 11 annotations, respectively, as being specific for these tissues (Figure 4b). Itaconate was one of the markers specific for the LPS-treated slice cultures[12b] (Figure 4c). Immunofluorescence histology with anti-CD68 (red) and Hoechst stain (blue) performed after MSI identified CD68-positive cells only in LPS-treated tissue with apparent co-localization with a subset of itaconate-positive cells. As expected, itaconate was not observed in the VEH and CLO slices (Figure 4c).

We compared microglia-containing slices (VEH and LPS) with microglia-depleted tissue (CLO) and identified 13 putative microglia metabolite markers, e.g., *m/z* 191.02 (citrate/isocitrate) indicating an active TCA cycle (Figure 4d). 20 marker candidates from the VEH versus LPS comparison (Figure 4b) were used to generate an activation/non-activation microglia-specific profile that was then compared to the markers found in cell culture (Figure 4e). 11 out of 20 of the slice culture-derived activation marker candidates (all [M-H]⁻) showed the same trend (up or down after LPS-treatment) in hiPSC (9 out of 20 for SIMA9): *m/z* 102.06 (GABA), *m/z* 115.00 (fumarate), *m/z* 129.02 (itaconate), *m/z* 130.05 (N-acetyl-alanine), *m/z* 131.08 (ornithine), *m/z* 134.05 (adenine), *m/z* 135.03 (hypoxanthine), *m/z* 146.05 (glutamate), *m/z* 174.04 (N-acetyl-aspartate; NAA), *m/z* 281.25 (FA18:1 as general cell marker), *m/z* 346.06 (AMP). 6 out of 8 *m/z* features that shared a trend between SIMA9 and hiPSC translated to rat hippocampal slice cultures: *m/z* 102.06 (GABA), *m/z* 115.00 (fumarate), *m/z* 129.02 (itaconate), *m/z* 131.08 (ornithine), *m/z* 135.03 (hypoxanthine), *m/z* 146.05 (glutamate), but not *m/z* 171.01 (glycerol phosphate) and *m/z* 214.05 (glycerol-3-phosphoethanolamine; Figure 4e). M3C clustering allowed for identification of common markers in slice culture and cell culture such as GABA (*m/z* 102.06) and glutamate (*m/z* 146.05), which were not discernible using bulk analyses (Figure 3h; Figures S26 and S27, Supporting Information).

All annotations were validated by accurate mass determination using magnetic resonance MS with <1 ppm mass accuracy and using MS2 fragment spectra-based annotation using SIRIUS[27] (Tables S1–S3, Supporting Information). In contrast to larger metabolites like lipids where ion mobility differences of isobaric compounds can be exploited for imaging prm-PASEF-based fragmentation analysis, small metabolites <300 Da cannot be resolved well by ion mobility. Therefore, we employed QTOF mode fragmentation analysis. For MS2 identification of GABA other isomers (dimethylglycine, 3-aminoisobutyrate, 2-aminobutanoate, or 3-aminoisobutanoate) cannot be ruled out. Because of the high brain concentrations and biological relevance
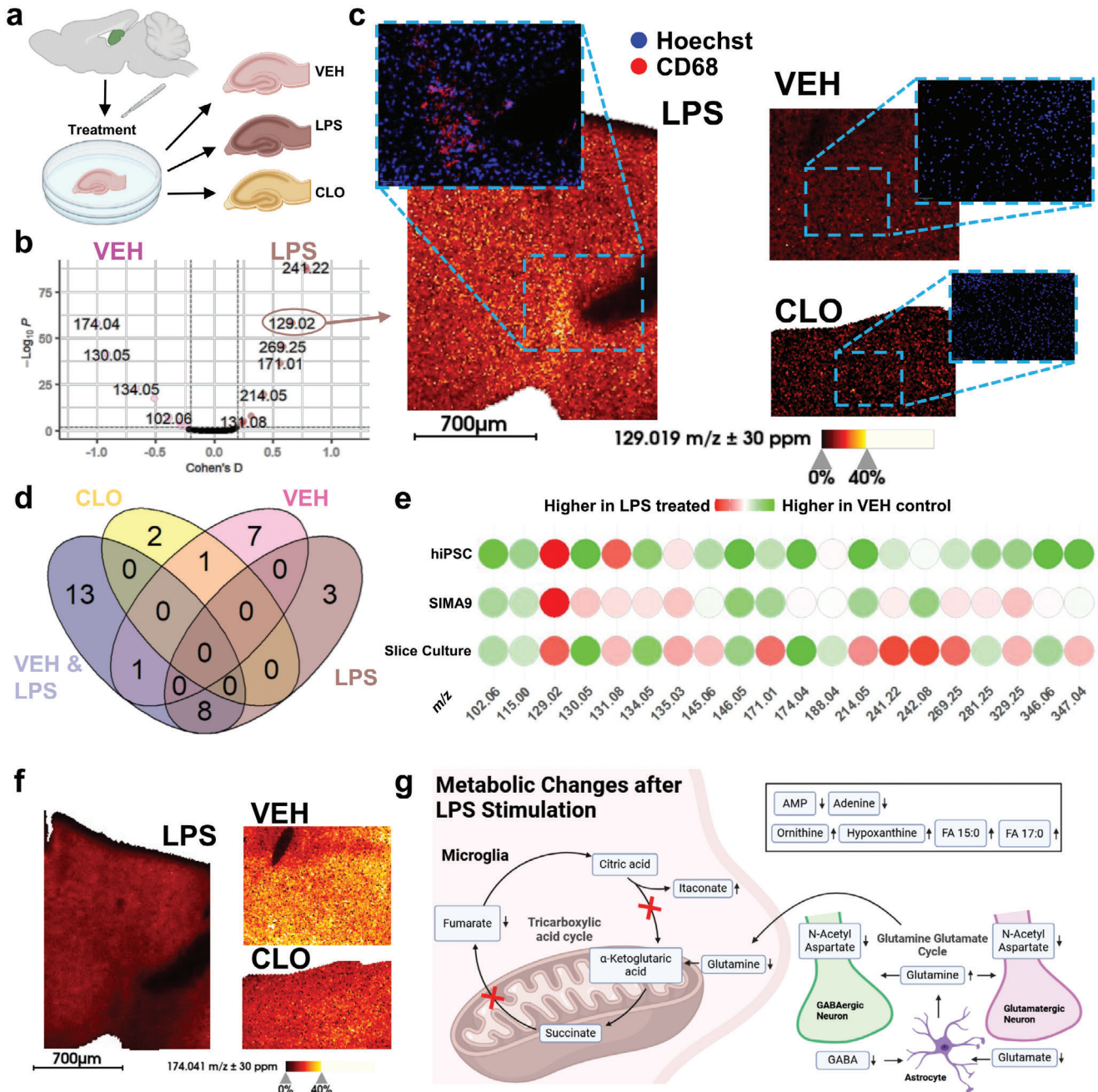
ADVANCED
SCIENCE NEWS

www.advancedsciencenews.com

ADVANCED
SCIENCE
Open Access

www.advancedscience.com

Figure 4. MALDI MS imaging of hippocampal slice cultures suggests metabolic neuron-glia interplay in response to LPS-induced neuroinflammation. a) Rat hippocampal slice cultures following 72 h incubation with different treatments: vehicle-treated (VEH), 1 µg mL^{-1} lipopolysaccharide (LPS), or 100 µg mL^{-1} clodronate (CLO, a bisphosphonate for selective macrophage and microglia depletion).[29a,b] b) Volcano plot comparing VEH- and LPS-treated hippocampal slices revealed m/z features that mark non-activated and LPS-responding cells. Measurements were taken from n = 5 animals with 3 replicates per treatment, for a total of 30 sections. Benjamini Hochberg adjusted p-value threshold was set to 0.01 and Cohen´s D threshold to ± 0.2. Itaconate (m/z 129.02; [M-H]$^-$) translates as a response marker from microglial cell populations (Figure 3) to slice cultures. c) Increased itaconate MSI ion intensities in LPS-treated hippocampal slices versus VEH and CLO controls (20 µm pixel size, negative ion mode). Anti-CD68-immunofluorescence overlay with Hoechst-stained nuclei suggests high microglia density in LPS-treated cultures. d) Metabolic profiling by MALDI MS imaging using KEGG METASPACE annotations at FDR<10%: Venn diagram comparing metabolites specific (Cohen´s D > 0.2 AND p < 0.01) for CLO slice cultures versus VEH&LPS cultures containing microglia. Then comparing LPS-treated slice culture against VEH. e) Comparison of slice culture with hiPSC and SIMA9 cell metabolite profiles, suggesting common markers of non-activated microglia: GABA*(m/z 102.06), fumarate (m/z 115.00), and glutamate (m/z 146.05) and of active microglia: Itaconate (m/z 129.02), ornithine (m/z 131.08) and hypoxanthine (m/z 135.03). The hiPSC profile shared non-activated markers N-acetyl-alanine (m/z = 130.05), adenine (m/z = 134.05), N-acetyl-aspartate (NAA) (m/z 174.04), FA 18:1 (m/z 281.25), and AMP (m/z 346.06) with slice cultures. f) Ion intensity of NAA is reduced in LPS-treated slice culture compared to VEH and CLO tissue. g) Hypothetical model of metabolic neuron-glia interplay in LPS-activated hippocampal slice cultures. In total five separate measurements were performed, with all three conditions measured in triplicates each time, resulting in 45 slice culture sections.

**ADVANCED
SCIENCE NEWS**

www.advancedsciencenews.com

**ADVANCED
SCIENCE**
Open Access

www.advancedscience.com

of GABA (4-aminoisobutanoate), it is the most likely molecule though.

Interestingly, NAA (*m/z* 174.04), one of the markers that was higher in non-activated cells and VEH tissue was also higher in microglia-depleted CLO tissue (Figure 4f). NAA, a very abundant and clinical magnetic resonance spectroscopy-accessible brain metabolite that neurons store in large quantities,[32] is also modulated by LPS in microglia. For several metabolites like glutamine (*m/z* 145.06), the trends for LPS-induced changes (up/down) did not match: Glutamine was lower in activated cell populations compared with non-activated cells, while LPS-treated tissue showed higher overall glutamine levels compared to the control tissue. This apparent contradiction may, however, be explained by the fact that slice cultures represent functional networks of different neural cell types, whereas our single-cell analysis exclusively focused on microglia-like cells.

It is tempting to speculate that co-localization of glutamine with itaconate in LPS-treated tissue (Figures S28 and S29, Supporting Information) could suggest that activated microglial cells (marked by itaconate) accumulate glutamine from other cell types in their vicinity in tissue slices. Metabolic flexibility enables microglial cells to utilize glutamine as an energy source.[33]

This capability is underscored by the upregulation of glutaminase during neuroinflammation, demonstrating their adaptation to use glutamine to meet energy demands.[34] The only source for glutamine in the brain is found in astrocytes, where glutamine synthetase converts glutamate to glutamine.[35] This conversion is part of the glutamine-glutamate cycle between neurons and astrocytes: The neurotransmitters GABA and glutamate are first taken up from the synaptic cleft by astrocytes and converted to glutamine. Then this glutamine is shuttled back to neurons to produce new neurotransmitters.[36] We also observed lower glutamate and GABA levels in slice and cell culture after LPS treatment, which may indicate that microglia that use glutamine as energy source may modulate the glutamine-glutamate cycle (Figures S28 and S29, Supporting Information). To expand this hypothesis, reduced NAA levels in LPS-treated tissue could indicate that the glutamate reservoir in neurons is depleted to feed microglial glutamine needs whilst also trying to retain neurotransmitter balance (Figure 4g). In analogy with cell cultures, there was a trend toward lower taurine after LPS treatment in slice cultures, but (unlike cell cultures) this decrease was not significant. Assuming that no taurine precursors were provided through the slice culture medium, taurine may – similar to glutamine – simply be replenished by another cell type in hippocampal slices, most likely astrocytes.[37]

Our data suggests a hypothetical model of metabolic neuron-glia interplay in LPS-activated hippocampal slice cultures that can be more extensively tested: Microglial activation by LPS interferes with the TCA cycle by producing itaconate instead of α-ketoglutarate. Itaconate, in turn, inhibits succinate dehydrogenase and fumarate generation in the TCA cycle.[12,38] To replenish the TCA cycle, glutamine, predominantly produced by astrocytes, is utilized as alternative energy source by microglia. Therefore, the glutamine-glutamate cycle between astrocytes and glutamatergic/GABAergic neurons may be impaired, leading to lower levels of glutamate and GABA in LPS-treated slice cultures. The observed decrease in NAA within LPS-treated slice cul-

tures could be a downstream effect, considering NAA's exclusivity to neurons, alongside its role as a "glutamate reservoir" that facilitates the regeneration of glutamate and GABA (Figures 4g and 5; Figure S30, Supporting Information). Our results also support the notion that single cell (type) studies in culture need to be interpreted with caution, since compensatory metabolic and metabolite shuttling mechanisms might apply in multi-cell type tissues.

3. Conclusion

With PRISM-MS and M3C we enable fast and metabolite-preserving single-cell MSI of a wide range of lipids and hydrophilic, low mass (<200 Da) metabolites in unfixed cells. We introduce GUVs as a qualitative ground truth concept for MALDI MS imaging and present MSI of slice cultures as a means for providing biological context for single cell studies. PRISM-MS analysis of LPS-dependent microglia activation highlights key changes of the itaconate-taurine ratio and of neuron-to-glia glutamate-glutamine shuttling. With its unique focus on small metabolites <200 Da that are fundamentally important for cell function and pathophysiology, PRISM-MS helps pave the way for single-cell low mass metabolomic analysis of cell subpopulations.

4. Experimental Section

Materials: The MALDI matrix 1,5-diaminonaphthalene (DAN), poly-L-lysine, Tween-20, MTT reagent (thiazolyl blue formazan), trifluoroacetic acid (TFA), Mayer's hemalaun solution, hydrochloric acid, sodium bicarbonate, magnesium sulfate, eosin Y-solution 0.5%, xylene, Biopore membranes, and Eukitt were purchased from Merck KGaA (Darmstadt, Germany). Acetonitrile (ACN), ethanol (EtOH), hydroxypropyl methylcellulose, ammonium formate, polyvinyl pyrrolidone, and LC-MS grade water were from VWR Chemicals (Darmstadt, Germany). ESI-L low concentration tuning mix for calibration of the timsTOF flex mass spectrometer's trap unit was used from Agilent Technologies (Waldbronn, Germany). Droplet-Micro-Array ITOs (DMA-ITOs) were acquired from Aquarray GmbH (Eggenstein-Leopoldshafen, Germany). Conductive indium tin oxide (ITO)-coated glass slides were sourced from Diamond Coatings (West Midlands, UK). BioGold microarray slides, Geltrex-coated surfaces, EDTA, DMEM/F12 with glutamine and HEPES, penicillin/streptomycin (PenStrep), Heat-inactivated fetal bovine serum (FBS), and heat-inactivated horse serum, Dulbecco's Balanced Salt Solution (DPBS), TrypLE Express, GlutaMAX supplement, 2-mercaptoethanol, and boronic acid were acquired from Thermo Fisher Scientific (Schwerte, Germany). From Sigma-Aldrich (Taufkirchen, Germany) L-Ascorbic acid 2-phosphate (LAAP), Hank's Balanced Salt Solution, lipopolysaccharide (LPS) from Escherichia coli O55:B5, insulin, transferrin, pluronic acid coating solution, polyethyleneimine (PEI), laminin, $MgCl_2$, $CaCl_2$, progesterone, putrescine, and sodium selenite were obtained. Sucrose, 1,2-dioleoyl-sn-glycero-3-phosphocholine (DOPC), 1,2-dimyristoyl-sn-glycero-3-phosphocholine (DMPC), and 1,2-Dioleoyl-sn-glycero-3-phosphoethanolamin-N-(lissamin-rhodamin B-sulfonyl) (LissRhod-PE) were purchased from Avanti Polar Lipids (Alabaster, United States). Indium tin oxide (ITO) coated glass slides, for GUV preparation, were purchased from Visiontek Systems Ltd. (Chester, United Kingdom). FGF-2 (154), TGF-β1, (ROCK) inhibitor Y-27632, VEGF-165, SCF, M-CSF, IL-3, and GM-CSF were obtained from Cell Guidance Systems (Cambridge, UK). Sarstedt (Nümbrecht, Germany) provided 6-well plates and U-bottom 96-well plates. Silicone grease Rotisilon C/D was purchased from Carl Roth (Karlsruhe,
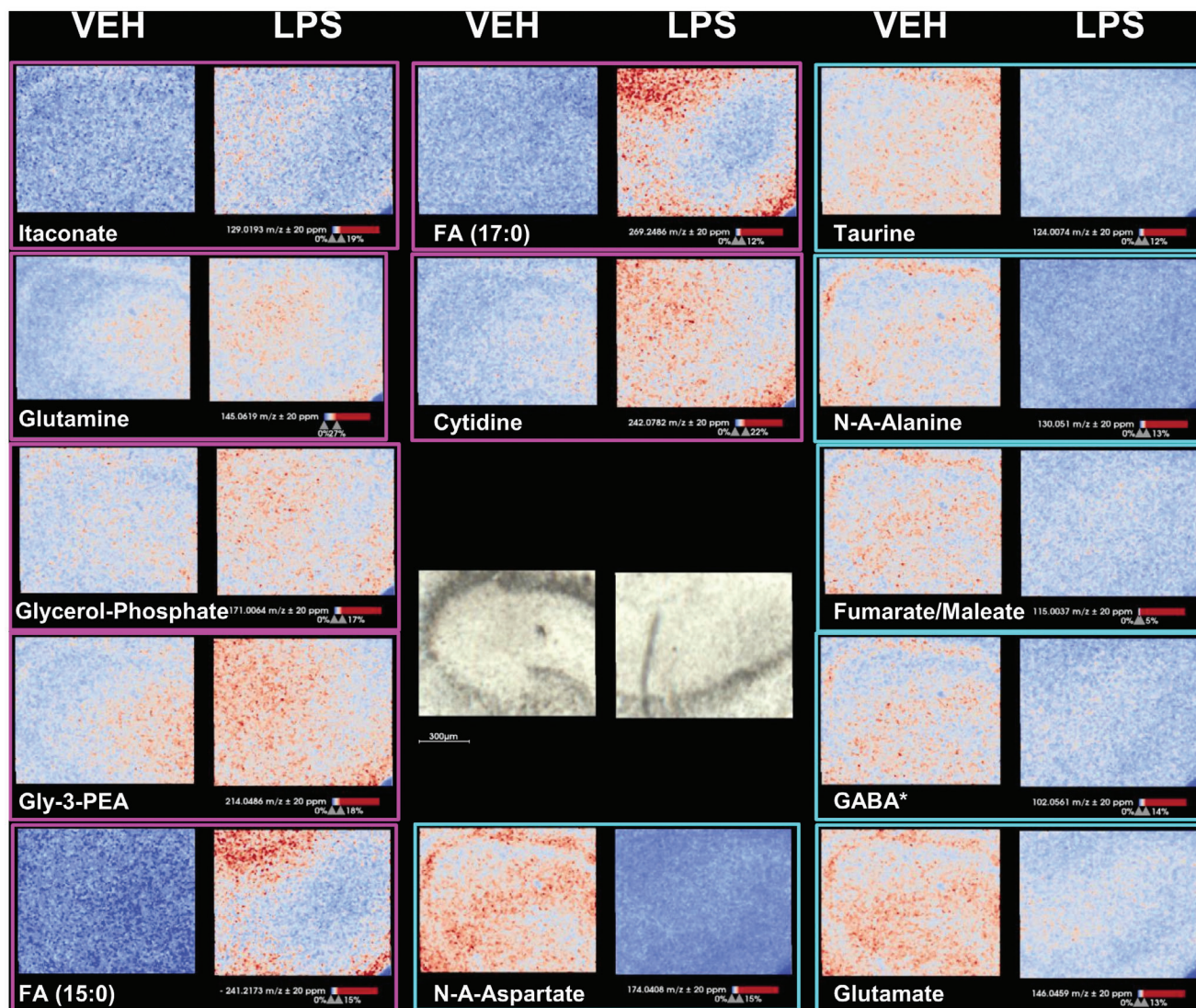
Figure 5. MALDI MS imaging reveals metabolic changes in hippocampal slice cultures. MALDI MS imaging of rat hippocampal slice cultures treated with vehicle (VEH) or with 1 µg mL^{-1} LPS at 5 µm pixel size. Ion images of metabolites that were significantly increased (magenta) or decreased (turquoise) between VEH and LPS groups (Tables S1–S3, Supporting Information). For orientation, a bright field image of both tissue areas is included in the middle. Metabolites marked with an asterisk where inconclusive in tandem MS as well as analysis of the resulting spectra using SIRIUS.

Germany). Other materials included BMP4 and IL-34 from Miltenyi Biotec (Bergisch Gladbach, Germany), X-VIVO15 from Lonza (Basel, Switzerland), and a 30 µm cell strainer from neoLab Migge GmbH (Heidelberg, Germany). Cell culture media included DMEM/F12, DMEM, PBS, and EMEM from Capricorn Scientific (Ebsdorfergrund, Germany). 8-well chambers from IBIDI (Gräfelfing, Germany) were used. TNF-α levels were measured with a murine TNF-α ABTS ELISA Development Kit from PeproTech (ThermoFisher, Darmstadt, Germany). The ELISA buffer Kit was purchased from PeproTech. For slice cultures, LPS from E. coli R515 was sourced from Enzo Life Sciences GmbH (Lörrach, Germany). Clodronate liposomes came from Liposoma B.V. (Amsterdam, Netherlands).

Cell lines and Animal Tissues: SIMA9 mouse microglia cells (Cat. No. CRL-3265), EOC 13.31 mouse microglia cells (Cat. No. CRL-2468), and LADMAC macrophages (Cat. No. CRL-2420) were obtained from ATCC (Manassas, United States). hiPSC lines hiPSC1 (male) and hiPSC1 (female) were used for microglial differentiation. Wistar rats were purchased

from Janvier (Le Genest-Saint-Isle, France) and treated in accordance with the European directive 2010/63/EU and the ARRIVE guidelines. Consent of the animal welfare officers at the University of Heidelberg was obtained (license T37/21).

Generation, Culture, and LPS-Treatment of hiPSC-Derived Microglia: All cells were maintained in humidified incubators at 37 °C and 5% CO$_2$. hiPSCs were cultured as colonies on Geltrex-coated (15 mg mL^{-1}) 6-well plates. Geltrex was thawed on ice, diluted 1:50 in wash medium, and subsequently added to tissue culture plates overnight at 4 °C for coating. hiPSCs were cultured in DMEM/F12 with glutamine and HEPES supplemented with Pen/Strep 1% (v/v), LAAP (64 µg mL^{-1}), sodium selenite (14 ng mL^{-1}), insulin 20 (µg mL^{-1}), transferrin 11 (µg mL^{-1}), FGF-2 100 (ng mL^{-1}), and TGF-β1 (2 ng mL^{-1}) with daily medium changes. Cells were passaged every 4–7 days at a 1:6 ratio using EDTA (0.5 mм) in DPBS. EDTA-containing liquid was aspirated, and hiPSCs were resuspended in hiPSC medium which was supplemented with the Rho-associated, coiled-coil containing protein kinase (ROCK) inhibitor Y-27632 for 24 h after split-

ting to promote cell survival. Generation of hiPSC-derived microglia was based on published work with minor adaptations.[39] hiPSCs were dissociated to single cells with TrypLE Express, resuspended in wash media, and centrifuged at $1200 \times g$ for 3.5 min. Cells were resuspended in EB medium (hiPSC medium supplemented with BMP4 50 ng mL^{-1}, VEGF-165 (50 ng mL^{-1}), SCF (20 ng mL^{-1}), Y-27632 (20 µM)) and plated into U-bottom 96-well plates at a density of 20000 cells / well to form embryoid bodies (EBs). Cell numbers were determined using an automated Luna cell counter (Luna, Nümbrecht, Germany). Prior to cell seeding, U-bottom 96-well plates were coated with pluronic acid coating solution at RT for 15 min. A 50% media change was performed on day 2 and on day 4 EBs were replated into non-coated 6-well plates with 15 EBs / well using 1250 µL pipette tips (Sarstedt, Nümbrecht, Germany) that were manually cut to increase the diameter size and reduce the shear force on the EBs. All remaining EB medium was removed, and EBs were supplied with 3 mL / well macrophage progenitor medium X-VIVO15 supplemented with Pen/Strep 1% (v/v), GlutaMAX supplement % (v/v), 2-mercaptoethanol (50 µM), M-CSF (100 ng mL^{-1}) and IL-3 (25 ng mL^{-1}). Medium was changed every 3 to 5 days depending on the consumption. Macrophage progenitor cells appeared in the supernatant after 3–4 weeks and could be harvested for many weeks, up to a few months. For maturation of microglia in monoculture, progenitor cells were harvested, filtered through a 30-µm cell strainer, and plated on gold slides with IBIDI Chambers on top at a density of 4000 cells / chamber. Prior to cell seeding, slides were coated with polyethyleneimine (1% v/v) and laminin (1 mg mL^{-1}). For coating, slides were first incubated with PEI coating solution (diluted 1:2000 in borate buffer (Boronic acid in H$_2$O, adjust pH to 8.4 with NaOH, 25 mM)) for 10 min at RT. After washing 3 x with H$_2$O, laminin (diluted 1:400 in DPBS + MgCl$_2$ and CaCl$_2$) was added overnight at 4 °C. IBIDI chambers were placed on top of the slides. Macrophage progenitor cells were differentiated into mature microglia over a course of 1 week in macrophage maturation medium (Pen/Strep 1% (v/v), GlutaMAX supplement 1% (v/v), 2-mercaptoethanol 50 µM, N2-supplement (DMEM/F12 with glutamine) 70% (v/v), Pen/Strep 1% (v/v), insulin (500 µg mL^{-1}), progesterone (630 ng mL^{-1}), putrescine (1.611 mg mL^{-1}), sodium selenite (520 ng mL^{-1}), transferrin (10 mg mL^{-1}), IL-34 (100 ng mL^{-1}) and GM-CSF (10 ng mL^{-1})). Half of the IBIDI chambers per slide received a treatment with 500 ng mL^{-1} LPS in DPBS for 24 h. Subsequently, the cell culture medium was aspirated, and the chambers were washed 3 x with ammonium formate buffer (150 mM) at 4 °C. This was followed by immediate snap-freezing of the slides in liquid nitrogen, ensuring that the slides did not come into direct contact with the liquid nitrogen by using an aluminum foil boat. IBIDI chambers were removed, and the slides were stored at −80 °C until further use.

Slice Culture Preparation, Treatment, and Cryosectioning: Organotypic hippocampal slice cultures were prepared as reported previously.[30] In brief, hippocampal slices (400 µm) were cut with a McIlwain tissue chopper (Mickle Laboratory Engineering Company Ltd., Guildford, UK) from male rats at postnatal day nine (P9) under sterile conditions. No antibiotic was added. Three slices were placed on semipermeable Biopore membranes, at the interface between serum-containing culture medium and humidified normal atmosphere enriched with 5% CO$_2$ (36.5 °C) in an incubator (Heracell, Thermo Fisher Scientific). The culture medium, exchanged three times per week, consisted of: 50% minimal essential medium (MEM), 25% Hank's balanced salt solution, 25% heat-inactivated HS, and L-glutamine (2 mM) at pH 7.3 (titrated with Trisbase). The glucose concentration of the culture medium was 4 mM glucose. Slice cultures (group LPS) were stimulated at DIV 9 for 72 h to bacterial LPS (1 µg mL^{-1}) (from Escherichia coli, serotype R515 (Re)). Slice cultures (group CLO) were exposed for twelve days-in-vitro (DIV) to liposome-encapsulated clodronate to deplete the microglial cell population.[29c] Liposomal clodronate was continuously present in the culture medium at a final concentration of 100 µg ml^{-1} from DIV 0 onward.[29d,30] Slice Cultures were snap-frozen on an aluminum block and stored at -80 °C. Prior to use, frozen slice cultures were placed in a cryostat (Leica CM1860 UV, Nuss-

loch, Germany), where 15 µm cryosections were prepared and mounted onto ITO slides for measurement. The chamber temperature was set to −20 °C.

Giant Unilamellar Vesicle (GUV) Preparation and Slide Preparation: GUVs were created by electroformation[40] in a Vesicle Prep Pro device (Nanion Technologies GmbH, Munich). Lipids in chloroform were mixed at the desired ratios and 40 µL of 5 mM lipid mix was spread onto the conductive side of an ITO (indium tin oxide)-coated slide. The slide was left under vacuum in a desiccator for 30 min to evaporate the chloroform. Afterward, a rubber ring was covered in silicone grease and positioned onto the spread lipids. 275 µL of sucrose solution (320 mM) were heated to 60 °C and filled inside the ring. A second ITO slide was placed on top of the ring with the conductive side facing down and the slides were connected to the respective electrodes inside the Vesicle Prep Pro. The Standard program that applies an AC field (3 V, 5 Hz) for 138 min was run at different temperatures. For the lipid mix containing 99% DOPC and 1% LissRhod-PE, the temperature was set to 37 °C and the GUVs were collected immediately after. For the other lipid mixes (99% DMPC, 1% LissRhod-PE and 49.5% DOPC, 49.5% DMPC, 1% LissRhod-PE), it was set to 70 °C and the GUVs were collected after 5 h when the chamber reached room temperature (RT) and slowly cooled to 12 °C in a thermoshaker (MKR 23, Hettich Benelux, Geldermalsen) over 1 h. All GUVs were eventually stored at 4 °C. GUVs were diluted 1:2000 in sucrose and pipetted onto ITO-Slides. These slides were coated using 4% BSA beforehand. These were then imaged with an LMD7000 laser microdissection microscope (Leica Microsystems, Wetzlar, Germany), where fluorescence signals were measured using the 515–545 nm emission filter channel at 10x magnification.

PRISM-MS MALDI Imaging: *Slide Preparation for Single-Cell MALDI-MS Imaging Metabolomics*: Gold-coated microarray slides were initially cleaned by sonication in three different solutions: acetone, methanol, and ddH$_2$O, each for 10 min, followed by air-drying in a desiccator. For calibration, teach marks were applied to the slides, which were then scanned using a CanoScan 8800F (Canon, Tokyo, Japan) slide scanner operated with Silverfast software. The slides were sterilized using 80% ethanol and dried under a sterile bench. They were then coated with sterile 0.01% (w/v) poly-L-lysine for 5 min at RT. After coating, slides were washed thrice with sterile ddH$_2$O and dried again under sterile conditions for 2 h.

Sample Preparation: Frozen slides were inserted into a lyophilization device, the Alpha 1–2 LDplus (Christ, Osterode, Germany), and dried for 60 min. Immediately following this drying step, for the PRISM-MS workflow, the matrix was directly applied by spray-coating. To mimic published optically guided workflows for comparative analysis with the PRISM-MS workflow, a second slide was positioned in a sterile hood at room temperature for 30 min prior to matrix spray-coating.

Matrix Spray-Coating: 1,5-Diaminonaphthalene (DAN) matrix solution (10 mg mL^{-1}) was prepared in ACN/ H$_2$O/Trp-D5 (60:39:1, v/v/v). Trp-D5 (from 5 mg mL^{-1} stock) was used as internal standard. Matrix solutions were sonicated for 15 min and deposited in eight spraying cycles onto slides using an M5 Sprayer (HTX Technologies LLC, Chapel Hill, USA). The spraying parameters were as follows: solvent composition was 60% ACN in water; nozzle temperature 70 °C; and bed temperature at 35 °C; flow rate at 0.07 mL min^{-1} with a nozzle velocity of 1200 mm min^{-1}. The track spacing was maintained at 2 mm in a HH pattern. The spraying pressure was 10 psi, and the gas flow rate was 2 L min^{-1}. There was no dry time involved in the process. The height of the nozzle from the slide surface was set at 40 mm. Following matrix-coating, slides were immediately placed in the mass spectrometer.

PRISM MS PreScan: PreScans at 200 µm pixel size were performed using the methods listed using an orthogonal TimsTOF flex mass spectrometer (Bruker Daltonics) in QTOF mode with flexImaging 7.4 software (Bruker Daltonics).

**ADVANCED
SCIENCE NEWS**

www.advancedsciencenews.com

**ADVANCED
SCIENCE**
Open Access

www.advancedscience.com

Parameter	PreScan (Cells or Tissue)	DeepScan (Cells or Tissue)	PreScan (GUVs)	DeepScan (GUVs)
Polarity	negative	negative	positive	positive
Range (m/z)	50-700	50-700	400-950	400-950
Laser shots	20	150	20	200
Laser frequency (1/s)	10000	10000	10000	10000
Laser field size (µm)	200×200	20×20	200×200	20×20
Funnel 1 RF (Vpp)	150	150	420	420
Funnel 2 RF (Vpp)	160	160	400	400
Multipole RF (Vpp)	170	170	380	380
Collision Energy (eV)	3	3	10	10
Collision RF (Vpp)	500	500	1800	1800
Low m/z	70	70	300	300
Transfer Time (µs)	40	40	85	85
Pre Pulse Storage (µs)	4	4	10	10

For tissue and cell measurements, the instrument was calibrated using ESI tune mix as calibrant and single point online calibration using a matrix peak of 1,5-DAN [M-H]$^-$ at m/z 157.0771. For measurements of GUVs in positive ion mode, red phosphorous was used as calibrant without additional online calibration. The laser was set to custom for PreScans with smart beam set to M5 and Beam Scan to on. The scan range was set to 126 resulting in a field size of 200 µm. The 20 µm DeepScans were performed using default 20 µm imaging laser settings. MS2 spectra were acquired using the same method as for the DeepScan with an m/z selection window of 0.5 m/z and collision energies varying between 5–30 V. The resolution was 30000 at m/z 208.1140.

PRISM-MS Data Processing, Data Storage, and DeepScan: The timsTOF flex MS imaging.tdf files were converted into.imzML files through *timsconvert* with a precision of 32 bit, excluding ion mobility and without compression.[41] The.imzML and corresponding.mis files were then analyzed by the following PRISM-MS R-script:

i. PreScan imaging data in.imzML format is loaded with a tolerance of 10 ppm using the Cardinal open-source software.[42] Additionally, the .mis-file created by the PreScan is loaded using the R-package *xml2* (https://github.com/r-lib/xml2) to parse the file. The script identifies predefined molecular peaks, such as the 281.2485 m/z peak corresponding to ubiquitous FA 18:1 used for targeting in single cells. (ii) A threshold κ defined as

$$k = \bar{l} + \alpha \cdot \sigma \tag{1}$$

where $\bar{l}$ denotes the mean intensity of a given m/z feature per ion image, σ the standard deviation and α being an integer value, is then applied to these peaks to generate a mask that highlights pixels where the peak is present, thus indicating areas of interest within the sample. The threshold can be adjusted manually, but defaults is set to $\alpha = 1$.

i. This mask is converted into a binary image aligned with the original flexImaging coordinates, thus allowing for definition of regions of interest (ROIs). It integrates the .mis file information with the .imzML

data coordinates, and the binary image is resized to match the resolution specified in the .mis file. An optional ROI dilation step is included, set by default to 1, indicating no change. (iv) Contours of these ROIs are derived from the thresholded image and then used as ROI coordinates for the subsequent DeepScan. Each contour defines a new imaging region, which is recorded in a newly generated .mis file. This new .mis file is a modification of the original, updating the measurement method name and incorporating the new raster size and coordinates for each new ROI. (v) This file can then be directly loaded into flexImaging for targeted data acquisition within the specified ROI.

MSI data was converted to .imzML-files again, which were then uploaded to the false discovery rate (FDR) controlled Metaspace database for annotation using HMDB (endogenous) and KEGG pathway databases.[19] Annotations with FDR ≤10% were then exported as a .csv file to store all annotations. An in-house R-script reduced the extracted .imzMLs to the annotated peaks with a tolerance of ± 0.005 Da with the help of the Cardinal R package for data storage until further processing.[42]

On-Tissue timsTOF MS2 Data Analysis: MS2 fragmentation spectra files were opened using DataAnalysis (Bruker Daltonik) and directly exported as .mgf files. These files where then loaded into and evaluated with SIRIUS Version 5.8.6.[27]

MALDI Magnetic Resonance MSI (MR-MSI): Ultra-high resolving power data was acquired on a solariX 7T XR Fourier Transform Ion Cyclotron Resonance (FT-ICR) mass spectrometer (Bruker Daltonics), equipped with a smartbeam II 2 kHz laser and ftms control 2.3.0 software (Bruker Daltonics, Build 92). Mass spectra were acquired in negative ion mode (m/z range 71.66–1000) and a time domain of acquisition of 8 M, resulting in long free induction decay (FID) times of 1.39 s and a mass resolution of 700000 at m/z 208.1140. Ion optics settings were constant for all measurements: funnel RF amplitude (1000 Vpp), source octopol (5 MHz, 350 Vpp), and collision cell voltage: 0 V, cell: 2 MHz, 1000 Vpp). The source DC optics was also constant for all measurements (capillary exit: −150 V, deflector plate: -200 V, funnel 1: −150 V, skimmer 1: −15 V), as well as the ParaCell parameters (transfer exit lens: 20 V, analyzer entrance: 10 V, sidekick: 0 V, side kick offset: 1.5 V, front/back trap plate: −2.8 V, back trap plate quench: 30 V). Sweep excitation power for ion detection was set to 14%, and ion accumulation time was 0.05 s. For IMP and ISOM, the transfer optics were as follows: time of flight: 0.4 ms, frequency: 6 MHz, and RF amplitude: 350 Vpp. The laser parameters were laser power: 30%, laser shots: 150, laser frequency: 2000 Hz, and laser focus: medium, at a lateral step size of 40 µm.

Statistical Analysis: *Single Cell and GUV Data Analysis*: Annotated and peak-picked .imzML files for single cell analysis were processed using an in-house R script, employing the Cardinal package for loading mass spectrometry (MS) data[42]: i) the script first extracts labels, constructs an intensity matrix, and stores essential image metadata such as pixel coordinates. ii) Data normalization is performed against the internal standard (IS) Trp-D5 (m/z 208.1140) by dividing the ion intensity at each point in a matrix $M \in \mathbb{R}^{i \times j}$ by the Trp-D5 intensity in the same spectrum. Here, each row i in the intensity matrix M corresponds to a distinct spectrum and each column j to unique m/z values. The normalization results in a new matrix M', representing normalized intensity values:

$$M_{i,j'} = \frac{M_{i,j}}{M_{i,Trp-D5}} \tag{2}$$

i. After normalization, Z-scale standardization is implemented for each m/z column. This standardization ensures a consistent scale across the entire dataset by adjusting the normalized intensity values. Specifically, each value is modified such that the distribution of intensities for each m/z feature has an average μ_j of zero and a standard deviation σ_j of one. A new matrix M'' represents normalized, scaled intensities:

$$M_{i,j''} = \frac{M'_{i,j} - \mu_j}{\sigma_j} \tag{3}$$

2410506 (12 of 15)

**ADVANCED
SCIENCE NEWS**

www.advancedsciencenews.com

**ADVANCED
SCIENCE**
Open Access

www.advancedscience.com

This two-step process corrects for potential discrepancies arising from sample handling, instrument performance, and other factors. Consequently, it enables more reliable comparison of molecule abundances across spectra. (iv) A cell-selection algorithm in the script then detects cell signal peaks such as m/z 281.2485 (or any other m/z chosen by the user). (v) Pixels with normalized and scaled intensities ≤ 3, for this feature, are removed from the imaging dataset. (vi) The remaining pixels are then processed through an algorithm that identifies and clusters connected pixels as cells, excluding clusters larger than 20 pixels. To focus on true single cells, it was shown that setting this to seven pixels excludes larger cell clusters. The script calculates and stores the mean spectrum for each cell cluster. This process is applied to all single cell measurements. For Giant Unilamellar Vesicles (GUV) processing, data underwent Total Ion Current (TIC) normalization, and the GUV-specific signals were the lipids DOPC $[M+H]^+$ (m/z 786.6) and DMPC $[M+H]^+$ (m/z 678.5). Here masks from both peaks are added together to pick GUVs, since there are no common peaks for both GUVs. Slice culture data was also normalized against Trp-D5 m/z 208.1140, then z-scale standardized and stored in a data frame for further processing.

Monte Carlo Consensus Clustering (M3C): Monte Carlo consensus clustering (M3C) was used for the analysis of cluster stability and for determination of the optimal number of clusters (k) for a given m/z-feature in a cell population.[24] This approach utilizes hierarchical clustering, conducted over five iterations per dataset on a single CPU core, ensuring methodological consistency. To guarantee reproducibility, a fixed seed value of 42 was used across all analyses. The analysis was restricted to a maximum of eight clusters (maxK) and executed 200 real and 200 reference iterations per cluster number (k) to evaluate the Relative Cluster Stability Indices (RCSI) and to calculate p-values. The RCSI metric was used to measure the stability of clustering outcomes, reflecting the consistency of sample groupings across multiple iterations; higher RCSI values indicate greater clustering stability. The significance of each cluster number was assessed based on p-values, with a threshold set at less than 0.01 indicating statistically significant clustering distinct from random chance. The optimal k was selected based on the highest RCSI among all k values with a p-value lower than 0.01. If no k values met this significance criterion, it was concluded that the observed m/z-feature did not exhibit sub clustering, thus suggesting a homogeneous distribution across the studied population.

Volcano Plots Using Cohen´s D: Volcano plots were generated using in house R-code, which is included in the available processing script. For every feature of the data, i.e., for a given m/z-interval, a p-value was generated that was adjusted according to the Benjamini Hochberg criterion to account for high dimensionality of the data.[43] Cohen´s D effect size was calculated for each group using this script. Since the data was standardized, the standard deviation σ_{12} is 1 and μ_1 and μ_2 are the mean intensities for a given group.

$$Cohen's\ D = \frac{\mu_1 - \mu_2}{\sigma_{12}} \tag{4}$$

A peak was considered relevant, if the effect size was above +0.2 or below −0.2[44] and the corresponding adjusted p-value was below 0.05. For cell culture, all data points were chosen, since they were considered being independent cells. In the slice culture analysis, a sample of 1000 pixels was randomly selected for each condition from a total population of 1284814 pixels. This random selection process was repeated ten times. Subsequently, the mean *p*-values and mean effect sizes were calculated based on these statistical samples. This procedure was implemented to eliminate the statistical dependence between adjacent pixels, which could lead to artificially inflated *p*-values.

Supporting Information

Supporting Information is available from the Wiley Online Library or from the author.

Conflict of Interest

D.S. is an employee of GSK, the company that funded part of this study, as demanded by BMBF regulations. All other authors declare no competing interests.

Author Contributions

J.L.C. conceived the PRISM-MS concept, wrote all code, performed MSI experiments, analyzed MSI data, prepared Figures and contributed to the first draft of the manuscript. J.H. performed cell culture, LPS-stimulation and MSI experiments, ELISA, and she analyzed MSI data. T.B. performed MS2 experiments. S.S. suggested experiments and analyzed data. A.L. and O.K. conducted hippocampal slice culture experiments and compound treatment. S.M. and K.G. generated and characterized GUVs. J.J. and P.K. generated, propagated, and analyzed hiPSCs. P.L. generated droplet microarrays. D.S. and C.H. conceived the study and discussed results. C.H. provided infrastructure, supervised the overall study, conceived GUVs as a ground truth in MSI, suggested experiments and wrote the final manuscript. All co-authors contributed to and edited the manuscript.

Data Availability Statement

All data supporting the findings of this study, including the code and measurement data, are publicly available. The code and Dataset S1 can be accessed on GitHub: https://github.com/CeMOS-Mannheim/PRISM-MS, and the measurement data is hosted on Metaspace https://metaspace2020.eu/project/PRISM-MS.

Ethics Approval Statement

hiPSCs used in this study were generated from healthy donors. Donors gave written informed consent. All experiments with human material are in accordance with the declaration of Helsinki.

[1] a) S. Schulz, M. Becker, M. R. Groseclose, S. Schadt, C. Hopf, *Curr. Opin. Biotechnol.* **2019**, *55*, 51; b) S. Heuckeroth, A. Behrens, C. Wolf, A. Futterer, I. D. Nordhorn, K. Kronenberg, C. Brungs, A. Korf, H. Richter, A. Jeibmann, U. Karst, R. Schmid, *Nat. Commun.* **2023**, *14*, 7495; c) Y. R. Xie, D. C. Castro, S. S. Rubakhin, T. J. Trinklein, J. V. Sweedler, F. Lam, *Nat. Methods* **2024**, *21*, 521; d) L. Gruber, S. Schmidt, T. Enzlein, H. G. Vo, J. L. Cairns, Y. Ucal, F. Keller, D. Abu Sammour, R. Rudolf, M. Eckhardt, S. A. Iakab, L. Bindila, C. Hopf, *(Preprint) bioRxiv* **2023**. https://doi.org/10.1101/2023.12.14.571637

[2] a) E. S. Berman, S. L. Fortson, K. D. Checchi, L. Wu, J. S. Felton, K. J. Wu, K. S. Kulp, *J. Am. Soc. Mass Spectrom.* **2008**, *19*, 1230; b) A. Amantonico, P. L. Urban, S. R. Fagerer, R. M. Balabin, R. Zenobi, *Anal. Chem.* **2010**, *82*, 7394; c) E. J. Lanni, S. S. Rubakhin, J. V. Sweedler, *J. Proteomics* **2012**, *75*, 5036; d) E. K. Neumann, T. J. Comi, S. S. Rubakhin, J. V. Sweedler, *Angew. Chem., Int. Ed. Engl.* **2019**, *58*, 5910; e) L. Rappez, M. Stadler, S. Triana, R. M. Gathungu, K. Ovchinnikova, P. Phapale, M. Heikenwalder, T. Alexandrov, *Nat. Methods* **2021**, *18*, 799; f) T. Bien, K. Koerfer, J. Schwenzfeier, K. Dreisewerd, J. Soltwisch, *Proc. Natl. Acad. Sci. USA* **2022**, *119*, e2114365119; g) M. A. Muller, N. Zweig, B. Spengler, M. Weinert, S. Heiles, *Anal. Chem.* **2023**, *95*, 11672.

[3] a) P. C. Chan-Andersen, E. V. Romanova, S. S. Rubakhin, J. V. Sweedler, *J. Biol. Chem.* **2022**, *298*, 102254; b) M. R. Molenaar, M. Shahraz, J. Delafiori, A. Eisenbarth, M. Ekelof, L. Rappez, T. Alexandrov, *Front. Mol. Biosci.* **2022**, *9*, 1021889; c) T. J. Comi, E. K. Neumann, T. D. Do, J. V. Sweedler, *J. Am. Soc. Mass Spectrom.* **2017**, *28*, 1919.

[4] a) J. Krismer, J. Sobek, R. F. Steinhoff, R. Brönnimann, M. Pabst, R. Zenobi, *Single Cell Metabolism. Methods in Molecular Biology*, (Ed: B. Shrestha) vol 2064, Humana, New York, NY **2020**; b) E. Cuypers, B. S. R. Claes, R. Biemans, N. G. Lieuwes, K. Glunde, L. Dubois, R. M. A. Heeren, *Anal. Chem.* **2022**, *94*, 6180.

[5] Y. R. Xie, V. K. Chari, D. C. Castro, R. Grant, S. S. Rubakhin, J. V. Sweedler, *J. Proteome Res.* **2023**, *22*, 491.

[6] H. Zhang, Y. Liu, L. Fields, X. Shi, P. Huang, H. Lu, A. J. Schneider, X. Tang, L. Puglielli, N. V. Welham, L. Li, *Nat. Commun.* **2023**, *14*, 5185.

[7] K. Gopfrich, B. Haller, O. Staufer, Y. Dreher, U. Mersdorf, I. Platzman, J. P. Spatz, *ACS Synth. Biol.* **2019**, *8*, 937.

[8] a) D. V. Hansen, J. E. Hanson, M. Sheng, *J. Cell Biol.* **2018**, *217*, 459; b) B. Dejanovic, T. Wu, M. C. Tsai, D. Graykowski, V. D. Gandham, C. M. Rose, C. E. Bakalarski, H. Ngu, Y. Wang, S. Pandey, M. G. Rezzonico, B. A. Friedman, R. Edmonds, A. De Maziere, R. Rakosi-Schmidt, T. Singh, J. Klumperman, O. Foreman, M. C. Chang, L. Xie, M. Sheng, J. E. Hanson, *Nat. Aging* **2022**, *2*, 837; c) M. Schwabenland, W. Bruck, J. Priller, C. Stadelmann, H. Lassmann, M. Prinz, *Acta Neuropathol.* **2021**, *142*, 923; d) F. Leng, P. Edison, *Nat. Rev. Neurol.* **2021**, *17*, 157.

[9] R. C. Paolicelli, A. Sierra, B. Stevens, M. E. Tremblay, A. Aguzzi, B. Ajami, I. Amit, E. Audinat, I. Bechmann, M. Bennett, F. Bennett, A. Bessis, K. Biber, S. Bilbo, M. Blurton-Jones, E. Boddeke, D. Brites, B. Brone, G. C. Brown, O. Butovsky, M. J. Carson, B. Castellano, M. Colonna, S. A. Cowley, C. Cunningham, D. Davalos, P. L. De Jager, B. de Strooper, A. Denes, B. J. L. Eggen, et al., *Neuron* **2022**, *110*, 3458.

[10] a) R. Scholz, D. Brosamle, X. Yuan, M. Beyer, J. J. Neher, *Immunol. Rev.* **2024**, *323*, 209; b) I. Pesamaa, S. A. Muller, S. Robinson, A. Darcher, D. Paquet, H. Zetterberg, S. F. Lichtenthaler, C. Haass, *Mol. Neurodegener.* **2023**, *18*, 70; c) A. Fernandez-Blanco, C. Sierra, C. Tejido, M. Dierssen, *Int. J. Mol. Sci.* **2024**, *25*; d) N. Sun, M. B. Victor, Y. P. Park, X. Xiong, A. N. Scannail, N. Leary, S. Prosper, S. Viswanathan, X. Luna, C. A. Boix, B. T. James, Y. Tanigawa, K. Galani, H. Mathys, X. Jiang, A. P. Ng, D. A. Bennett, L. H. Tsai, M. Kellis, *Cell* **2023**, *186*, 4386; e) L. Schirmer, D. Velmeshev, S. Holmqvist, M. Kaufmann, S. Werneburg, D. Jung, S. Vistnes, J. H. Stockley, A. Young, M. Steindel, B. Tung, N. Goyal, A. Bhaduri, S. Mayer, J. B. Engler, O. A. Bayraktar, R. J. M. Franklin, M. Haeussler, R. Reynolds, D. P. Schafer, M. A. Friese, L. R. Shiow, A. R. Kriegstein, D. H. Rowitch, *Nature* **2019**, *573*, 75.

[11] A. M. Sabogal-Guaqueta, A. Marmolejo-Garza, M. Trombetta-Lima, A. Oun, J. Hunneman, T. Chen, J. Koistinaho, S. Lehtonen, A. Kortholt, J. C. Wolters, B. M. Bakker, B. J. L. Eggen, E. Boddeke, A. Dolga, *Nat. Commun.* **2023**, *14*, 6454.

[12] a) L. A. J. O'Neill, M. N. Artyomov, *Nat. Rev. Immunol.* **2019**, *19*, 273; b) B. Chausse, A. Lewen, G. Poschet, O. Kann, *Brain Behav. Immunity* **2020**, *88*, 802.

[13] L. Peruzzotti-Jametti, C. M. Willis, G. Krzak, R. Hamel, L. Pirvan, R. B. Ionescu, J. A. Reisz, H. A. Prag, M. E. Garcia-Segura, V. Wu, Y. Xiang, B. Barlas, A. M. Casey, A. M. R. van den Bosch, A. M. Nicaise, L. Roth, G. R. Bates, H. Huang, P. Prasad, A. E. Vincent, C. Frezza, C. Viscomi, G. Balmus, Z. Takats, J. C. Marioni, A. D'Alessandro, M. P. Murphy, I. Mohorianu, S. Pluchino, *Nature* **2024**, *628*, 195.

[14] S. Ahmed, N. Ma, J. Kawanokuchi, K. Matsuoka, S. Oikawa, H. Kobayashi, Y. Hiraku, M. Murata, *Sci. Rep.* **2024**, *14*, 7427.

[15] C. RamalloGuevara, D. Paulssen, A. A. Popova, C. Hopf, P. A. Levkin, *Adv. Biol.* **2021**, *5*, e2000279.

[16] Y. Li, L. M. Almassalha, J. E. Chandler, X. Zhou, Y. E. Stypula-Cyrus, K. A. Hujsak, E. W. Roth, R. Bleher, H. Subramanian, I. Szleifer, V. P. Dravid, V. Backman, *Exp. Cell Res.* **2017**, *358*, 253.

[17] a) S. Qin, Y. Zhang, M. Shi, D. Miao, J. Lu, L. Wen, Y. Bai, *Nat. Commun.* **2024**, *15*, 4387; b) S. Pan, C. Liu, H. Yao, X. Pan, J. Li, J. Yang, M. Du, P. Liu, S. Zhang, X. Zhang, *Chem. Commun.* **2024**, *60*, 392.

[18] S. Schuster, C. D. Johnson, M. Hennebelle, T. Holtmann, A. Y. Taha, I. A. Kirpich, A. Eguchi, C. E. Ramsden, B. G. Papouchado, C. J. McClain, A. E. Feldstein, *J. Lipid Res.* **2018**, *59*, 1597.

[19] A. Palmer, P. Phapale, I. Chernyavsky, R. Lavigne, D. Fay, A. Tarasov, V. Kovalev, J. Fuchser, S. Nikolenko, C. Pineau, M. Becker, T. Alexandrov, *Nat. Methods* **2017**, *14*, 57.

[20] X. Liu, W. Song, B. Y. Wong, T. Zhang, S. Yu, G. N. Lin, X. Ding, *Genome Biol.* **2019**, *20*, 297.

[21] M. Prasad, G. Postma, P. Franceschi, L. M. C. Buydens, J. J. Jansen, *Sci. Rep.* **2022**, *12*, 15687.

[22] T. Alexandrov, J. H. Kobarg, *Bioinformatics* **2011**, *27*, i230.

[23] B. Balluff, A. Buck, M. Martin-Lorenzo, F. Dewez, R. Langer, L. A. McDonnell, A. Walch, R. M. A. Heeren, *Proteom. Clin. Appl.* **2019**, *13*, e1800137.

[24] C. R. John, D. Watson, D. Russ, K. Goldmann, M. Ehrenstein, C. Pitzalis, M. Lewis, M. Barnes, *Sci. Rep.* **2020**, *10*, 1816.

[25] L. Ni, J. Xiao, D. Zhang, Z. Shao, C. Huang, S. Wang, Y. Wu, N. Tian, L. Sun, A. Wu, Y. Zhou, X. Wang, X. Zhang, *Cell Death Dis.* **2022**, *13*, 140.

[26] K. Liu, R. Zhu, H. Jiang, B. Li, Q. Geng, Y. Li, J. Qi, *Mol. Cell. Neurosci.* **2022**, *122*, 103759.

[27] K. Duhrkop, M. Fleischauer, M. Ludwig, A. A. Aksenov, A. V. Melnik, M. Meusel, P. C. Dorrestein, J. Rousu, S. Bocker, *Nat. Methods* **2019**, *16*, 299.

[28] a) K. M. Dave, L. Ali, D. S. Manickam, *PLoS One* **2020**, *15*, e0231597; b) M. Blank, T. Enzlein, C. Hopf, *Sci. Rep.* **2022**, *12*, 2908.

[29] a) L. A. Koennecke, M. A. Zito, M. G. Proescholdt, N. van Rooijen, M. P. Heyes, *J. Neurochem.* **1999**, *73*, 770; b) A. Kohl, F. Dehghani, H. W. Korf, N. P. Hailer, *Exp. Neurol.* **2003**, *181*, 1; c) A. Lewen, A. T. Ta, T. Cesetti, J. O. Hollnagel, I. E. Papageorgiou, B. Chausse, O. Kann, *J. Neurosci. Res.* **2020**, *98*, 1953; d) T. T. Ta, H. O. Dikmen, S. Schilling, B. Chausse, A. Lewen, J. O. Hollnagel, O. Kann, *Proc. Natl. Acad. Sci. USA* **2019**, *116*, 4637; e) B. Chausse, N. Malorny, A. Lewen, G. Poschet, N. Berndt, O. Kann, *Sci. Rep.* **2024**, *14*, 14405.

[30] I. E. Papageorgiou, A. Lewen, L. V. Galow, T. Cesetti, J. Scheffel, T. Regen, U. K. Hanisch, O. Kann, *Proc. Natl. Acad. Sci. USA* **2016**, *113*, 212.

[31] a) J. Vinet, H. R. Weering, A. Heinrich, R. E. Kalin, A. Wegner, N. Brouwer, F. L. Heppner, N. Rooijen, H. W. Boddeke, K. Biber, *J. Neuroinflammation* **2012**, *9*, 27; b) X. Han, Q. Li, X. Lan, L. El-Mufti, H. Ren, J. Wang, *Mol. Neurobiol.* **2019**, *56*, 6184.

[32] a) G. Tsai, J. T. Coyle, *Prog. Neurobiol.* **1995**, *46*, 531; b) F. Abbaspour, N. Mohammadi, H. Amiri, S. Cheraghi, R. Ahadi, Z. Hormozi-Moghaddam, *Heliyon* **2024**, *10*, e30521.

[33] L. P. Bernier, E. M. York, A. Kamyabi, H. B. Choi, N. L. Weilinger, B. A. MacVicar, *Nat. Commun.* **2020**, *11*, 1559.

[34] a) L. Ding, X. Xu, C. Li, Y. Wang, X. Xia, J. C. Zheng, *Brain Behav. Immunity* **2021**, *92*, 139; b) G. Gao, S. Zhao, X. Xia, C. Li, C. Li, C. Ji, S. Sheng, Y. Tang, J. Zhu, Y. Wang, Y. Huang, J. C. Zheng, *Front. Cell Neurosci.* **2019**, *13*, 264.

[35] M. D. Norenberg, A. Martinez-Hernandez, *Brain Res.* **1979**, *161*, 303.

[36] L. K. Bak, A. Schousboe, H. S. Waagepetersen, *J. Neurochem.* **2006**, *98*, 641.

[37] S. Ramirez-Guerrero, S. Guardo-Maya, G. J. Medina-Rincon, E. E. Orrego-Gonzalez, R. Cabezas-Perez, R. E. Gonzalez-Reyes, *Front. Mol. Neurosci.* **2022**, *15*, 937789.

[38] A. K. Jaiswal, J. Yadav, S. Makhija, S. Mazumder, A. K. Mitra, A. Suryawanshi, M. Sandey, A. Mishra, *Mucosal Immunol.* **2022**, *15*, 301.

[39] W. Haenseler, S. N. Sansom, J. Buchrieser, S. E. Newey, C. S. Moore, F. J. Nicholls, S. Chintawar, C. Schnell, J. P. Antel, N. D. Allen, M. Z. Cader, R. Wade-Martins, W. S. James, S. A. Cowley, *Stem Cell Rep.* **2017**, *8*, 1727.

[40] M. I. Angelova, D. S. Dimitrov, *Faraday Discuss. Chem. Soc.* **1986**, *81*, 303.

[41] G. T. Luu, M. A. Freitas, I. Lizama-Chamu, C. S. McCaughey, L. M. Sanchez, M. Wang, *Bioinformatics* **2022**, *38*, 4046.

[42] K. A. Bemis, M. C. Foll, D. Guo, S. S. Lakkimsetty, O. Vitek, *Nat. Methods* **2023**, *20*, 1883.

[43] Y. Benjamini, Y. Hochberg, *J. R. Stat. Soc.: Series B* **1995**, *57*, 289.

[44] Y. Yang, J. Cheng, S. Wang, H. Yang, *J. Proteomics* **2022**, *250*, 104386.